



# New insights into optical properties, and applications of Zr-doped BaTiO<sub>3</sub>

Mahasen Reda<sup>1</sup> · Ebtesam E. Ateia<sup>1</sup> · S. I. El-Dek<sup>2</sup> · M. M. Arman<sup>1</sup>

Received: 27 September 2023 / Accepted: 11 February 2024 / Published online: 21 March 2024  
© The Author(s) 2024

## Abstract

The present work scrutinizes a few uses of barium titanate BaTi<sub>1-x</sub>Zr<sub>x</sub>O<sub>3</sub> (0.0 ≤ x ≤ 0.3) nanoparticles, which are an innovative and highly promising material for a variety of applications, including optical applications; and waste water treatment. To estimate the quality of a synthesized powder relative to an already existing commercial powder, the samples were prepared using cheaper raw materials and simpler, faster procedures than those reported in other literature at lower annealing durations and temperatures. The prepared samples were characterized by field emission scanning electron microscopy (FESEM), and Raman spectroscopy, which confirmed the coarse nature of the samples and the system's tetragonality. Furthermore, UV–visible absorbance of all compositions was studied. It has been determined that optical transition is directly allowed after extensive research, and the optical band gap (E<sub>g</sub>) values increase with increasing (Zr<sup>4+</sup>) ion concentration. The derivation of absorption spectrum fitting (DASF) technique was used to support the type of transition and calculate the value of the coefficient of electronic transition (n). Samples can perform overall water splitting and CO<sub>2</sub> reduction processes. The Langmuir and Freundlich isotherms were used to comprehend the procedure of adsorption on the investigated samples. The BaTi<sub>0.8</sub>Zr<sub>0.2</sub>O<sub>3</sub> has been used to successfully remove 99.9% of heavy metals (Cr<sup>6+</sup>) from wastewater. The obtained results provide new insights into the control of the structure, and optical behaviors in BaTi<sub>1-x</sub>Zr<sub>x</sub>O<sub>3</sub>.

**Keywords** BaTiO<sub>3</sub> · Direct energy gap · Optical properties · Heavy metal removal · Adsorption process

## 1 Introduction

Barium titanate (BT) is a compound that has gained significant attention in the field of materials science and engineering due to its unique properties and wide range of applications. (BT) exhibits ferroelectric behavior, meaning it can switch its polarization in response to an applied electric field. This property makes it highly useful in various electronic devices such as capacitors, transducers, sensors, and memory devices. Its high dielectric constant also makes it suitable for use in multilayer ceramic capacitors (MLCCs), which are essential components in modern electronics [1]. Furthermore, (BT) has piezoelectric properties, allowing it

to convert mechanical stress into electrical energy and vice versa. This characteristic makes it valuable in applications like ultrasound transducers, actuators, acoustic devices [2, 3], and energy storage applications [4].

Many researchers have sought to improve the optical properties of various nano-compounds. Nadim Ullah et al. [5] successfully synthesized pure cobalt and cobalt doped MnO<sub>2</sub> nanorods using a simple hydrothermal method. The UV–visible absorption spectroscopy indicates a wide absorption band, centred at ~450 nm for pure and ~465 nm for cobalt-doped MnO<sub>2</sub> nanorods. The band gap decreased from 2.36 to 1.96 eV as the dopant concentration increased. Murtaza Saleema et al. [6] successfully synthesized homogeneous CdTe<sub>1-x</sub>Se<sub>x</sub> thin films (x = 0, 3.125%, 6.25%, and 12.5%) using a chemically produced sol–gel spin coating approach. The experimental energy gap was lowered from 1.84 eV for pure CdTe to 1.55 eV upon incorporating Se into the pristine structure. The addition of Se content into the lattice increases optical characteristics in the visible region. The findings of their work indicate that Se-containing CdTe compositions are promising candidates for

✉ Ebtesam E. Ateia  
drebtesam2000@yahoo.com; ebtesam@sci.cu.edu.eg

<sup>1</sup> Physics Department, Faculty of Science, Cairo University, Giza, Egypt

<sup>2</sup> Materials Science and Nanotechnology Department, Faculty of Postgraduate Studies for Advanced Sciences (PSAS), Beni-Suef University, Beni-Suef, Egypt

better thermoelectric and optoelectronic applications. Talat Zeeshan et al. [7] investigated Al-doped  $ZrO_2$  compositions using computational and experimental methods. They succeeded in reducing the energy band gap value for  $ZrO_2$  from 2.76 to 1.80 eV at different Al content. Mohammed Tauseef Qureshi et al. [8] reported that the refractive index of Ag-doped  $Cu_2O$  increases with photon energy, resulting in higher transmittance power. The band gaps decrease from 2.33 to 1.99 eV with Ag doping, which was attributed to a significant improvement in optical conductivity.

Over the last few decades, the entire globe has been concerned about heavy metal poisoning in water. Different organic pollutants are biodegradable due to their high toxicity and non-degradability [9]. ( $Cr^{6+}$ ) is one of the most harmful heavy metal ions. Several approaches, including ion exchange [10], the process of reverse osmosis [11], filtration via membranes [12], the technique of chemical precipitation [13], photocatalysis process [14, 15], and the adsorption process [16], have recently been employed for the treatment and re-use of polluted water contaminated by heavy metal ions. Adsorption is the most preferred approach among all previous procedures because of its economic cost, repeatability, and efficacy [17]. The heavy metal adsorption process is associated with both adsorbent and adsorbate. Heavy metal absorption in adsorbents is influenced by its concentration in the solution, contact time, and pH. Furthermore, the adsorbate is helpful in removing heavy metals.

Water treatment applications have attracted the attention of many researchers. The removal of heavy chromium ions from waste water has a large share in this study. Tshireletso M. Madumo et al. succeeded in preparing metal–organic framework-5/nitrogen-doped graphene (MOF-5/(x)NGO) nanocomposites bearing ( $Cr^{6+}$ ) adsorption properties. The ideal conditions for maximal ( $Cr^{6+}$ ) adsorption were determined to be pH = 2, contact time of 60 min, and adsorbent dose of  $6 \text{ mg}\cdot\text{L}^{-1}$ , starting ( $Cr^{6+}$ ) content of  $0.5 \text{ mg}\cdot\text{L}^{-1}$ , and temperature of  $30 \text{ }^\circ\text{C}$ . The composite MOF-5/(0.05 wt%) NGO attained a maximum adsorption efficiency of 46.1% [18]. Jing-Yi Liang et al. used passion fruit peel and  $FeCl_3$  solution to synthesize a novel fruit peel-based bio-char composite (FPBC) that was effectively employed as a sorbent to remove ( $Cr^{6+}$ ) from water. The findings of the trials revealed that FPBC had good removal performance on ( $Cr^{6+}$ ), with simultaneous removal efficiencies of 97% within 3 h [19].

The purpose of the current investigation is to evaluate the optical and morphological properties of  $BaTi_{1-x}Zr_xO_3$ . In addition, the authors also evaluated the ability of prepared nanoparticles (NPs) to remove heavy metal ( $Cr^{6+}$ ) from water.

## 2 Experimental techniques

### 2.1 Method of preparation of $BaTiO_3$ and Zr-doped $BaTiO_3$ nanoparticles (NPs)

$BaTi_{1-x}Zr_xO_3$  NPs were prepared using the modified citrate procedure. The precursors used were Barium Nitrate [ $Ba(NO_3)_2$ , 99.9%] (Sigma-Aldrich), tetrabutyl titanate [ $Ti(OC_4H_9)_4$ , 97%, Zirconium Oxochloride [ $ZrOCl_2$ , 99.9%] (Sigma-Aldrich), and citric acid. In separate beakers, 1-mol of  $Ba(NO_3)_2$  and 2-mol of citric acid were dissolved in enough deionized water to form complete solutions, and (x)-mol of  $ZrOCl_2$  solution was added to a (1-x)-mol of tetrabutyl titanate suspension and thoroughly mixed with the citric acid solutions on the magnetic stirrer at  $70 \text{ }^\circ\text{C}$  for 60 min. The  $Ba(NO_3)_2$  solution was added, and the pH was adjusted to 8. The mixture was heated to  $120 \text{ }^\circ\text{C}$  and stirred continuously until all of the volatile components and water had evaporated. After that, the mixture seemed somewhat thick and sticky, and it was allowed to burn entirely on the hot plate to produce a black, fine powder. Finally, the black powder was annealed at  $1100 \text{ }^\circ\text{C}$  at a rate of  $5 \text{ }^\circ\text{C}/\text{min}$  for 120 min [20].

### 2.2 Characterization techniques

The surface morphology of the samples was scanned using a field emission scanning electron microscope (FESEM) Model Quanta 250 FEG (Field Emission Gun). The 3D micrographs of the prepared  $BaTi_{1-x}Zr_xO_3$  NPs were processed using Gwyddion software (2.62). The roughness characteristics were investigated using ImageJ software to analyze topographical scans of the sample's surface. Room-temperature Raman analysis (RA) of  $BaTi_{1-x}Zr_xO_3$  (at  $x = 0.0$  and  $x = 0.2$ ) was studied using LabRAM HR-Evolution Raman Microscopy.

A UV–visible–NIR Spectrophotometer (JASCO Corp., V-570) was used to evaluate the optical absorption and transmission spectra of the samples before and after irradiation by laser in the spectral region 190–2500 nm.

### 2.3 Heavy metal removal

The optimum pH value was identified for the ion removal efficiency using Zr-doped  $BaTiO_3$  NPs. The studies took place in a sequence of 10-ml flasks with 20 mg/L contents of powdered NPs in a 50 ppm chromium ( $Cr^{6+}$ ) ion solution. Ammonia solution ( $NH_4OH$ ) and diluted nitric acid

were used to regulate metal ion solutions at pH levels ranging from 4 to 8. The examined solutions were thoroughly dispersed using an electric shaker (Orbital Shaker SO1) at 200 rpm for 1 h. Following that, the supernatant solutions were collected and filtered using a 0.2- $\mu$ m syringe filter. The HM content within the filtrate was determined by inductively coupled plasma (ICP) spectrometry (Prodigy7) at 25 °C. The following equations were used to compute the nano-material removal efficiency ( $\eta$ ) [13, 21] and the capability at equilibrium adsorption ( $q_e$ ) [22]:

$$\eta = \frac{C_i - C_e}{C_i} \times 100 \tag{1}$$

$$q_e = \frac{(C_i - C_e)V}{m} \tag{2}$$

where  $C_i$  and  $C_e$  are the starting and ending contents (mg/L) of the Cr<sup>6+</sup> ion in solution, respectively,  $m$  is the adsorbent mass,  $V$  is the volume of Cr<sup>6+</sup> solution, and  $q_e$  is the amount of metal ion adsorbed per specific amount of adsorbent (mg/g).

**Table 1** Roughness parameters: the average roughness ( $R_a$ ) root mean square roughness ( $R_q$ ), the maximum height of roughness ( $R_r$ ) and the crystallite size of BaTi<sub>(1-x)</sub>Zr<sub>x</sub>O<sub>3</sub>; (0.0 ≤ x ≤ 0.3) NPs

Composition	$R_a$ (nm)	$R_q$ (nm)	$R_r$ (nm)	USDM (nm)
$x=0.0$	21.68	50.10	255.80	25
$x=0.1$	15.63	40.92	255.36	29
$x=0.2$	19.54	46.59	256.54	25
$x=0.3$	19.92	47.75	256.23	28

### 3 Results and discussion

#### 3.1 XRD analysis

The XRD patterns of the samples with the formula BaTi<sub>(1-x)</sub>Zr<sub>x</sub>O<sub>3</sub> are displayed in Fig. 1 (0 ≤ x ≤ 0.3). The investigated samples crystallized with one molecule in each unit cell in a single phase with the tetragonal space group P4mm. As mentioned in the prior work [20], the Uniform Stress Deformation Model (USDM) is a simple method for estimating any deformation in the lattice structure and measuring the size of crystal structures. Table 1 displays the calculated crystallite size (D).

#### 3.2 Surface topography

FESEM was used to study the morphology of BaTi<sub>(1-x)</sub>Zr<sub>x</sub>O<sub>3</sub> (x = 0.0, 0.2), as shown in Fig. 2a. According to the images, the NPs appear to be tetragonal in shape, contain aggregates of grains, and have intragranular porosity, as mentioned in earlier research [20]. The FESEM micrographs were examined using Gwyddion 2.50 software. This process was utilized to examine the surface roughness (RFs) of the studied samples as illustrated in Fig. 2b, c where the addition of Zr at the expense of Ti reduced the RFs of the surface from 9.5 to 6.2 nm. This reduction is caused by NPs agglomeration and the high viscosity of the casting solutions [23]. The average roughness ( $R_a$ ) was used to investigate the surface roughness, which implies the arithmetic average of departures from the mean line in profile height. It is provided by the following equation [24]:

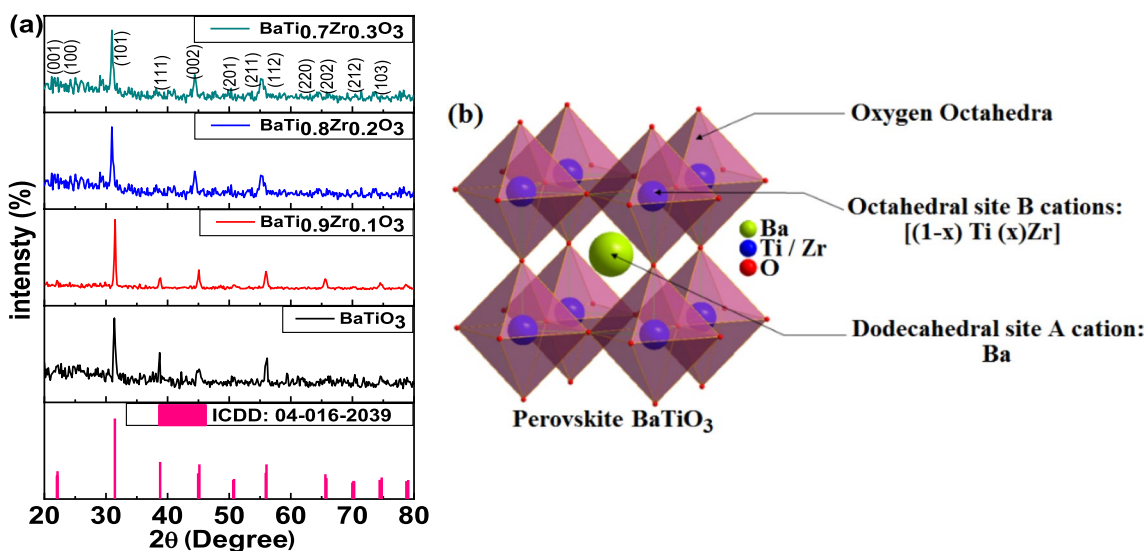


**Fig. 1** a XRD pattern and b crystal structure of BaTi<sub>(1-x)</sub>Zr<sub>x</sub>O<sub>3</sub> (0.0 ≤ x ≤ 0.3) [20]

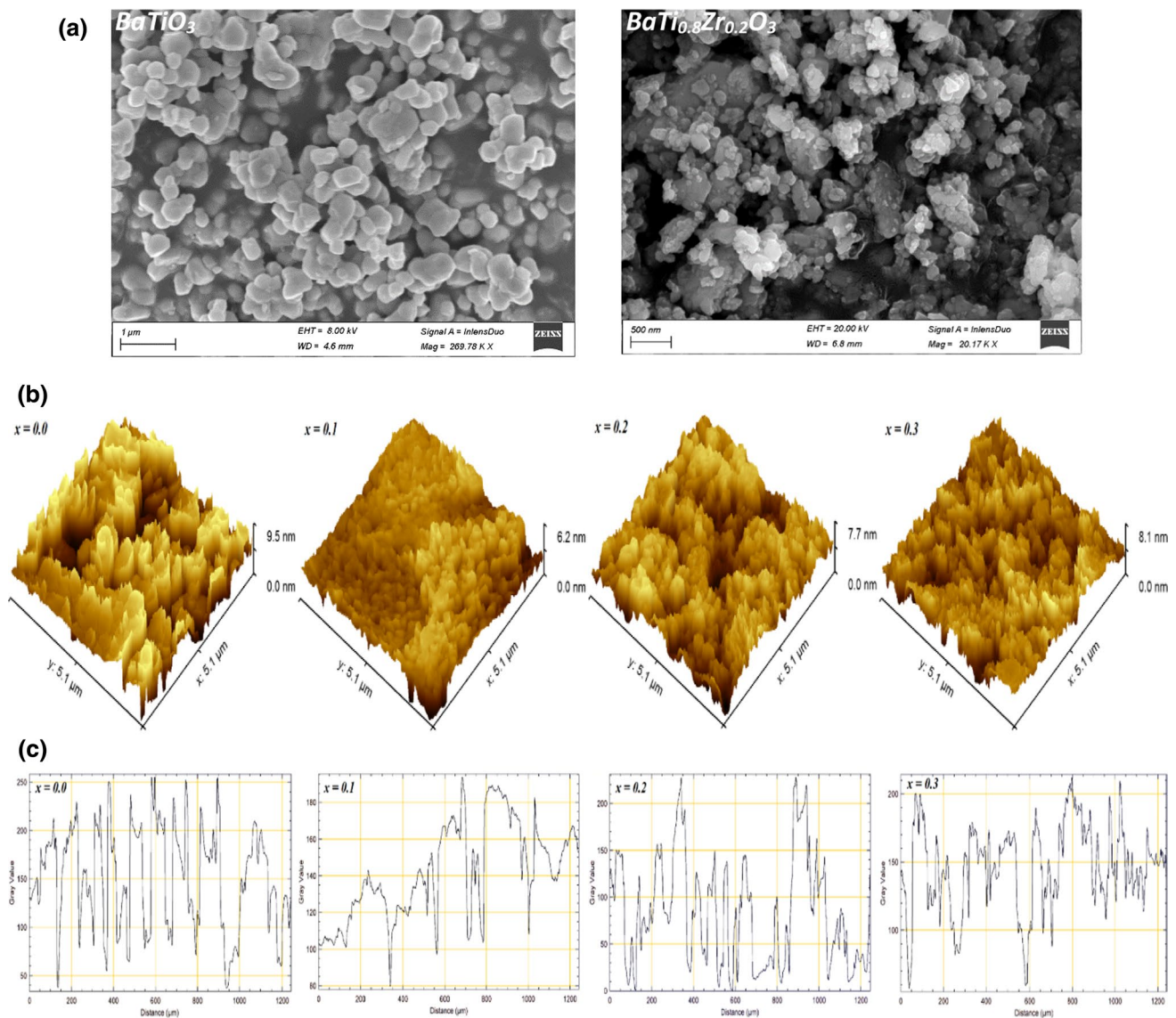


**Fig. 2** **a** The FESEM of BaTiO<sub>3</sub> and BaTi<sub>0.8</sub>Zr<sub>0.2</sub>O<sub>3</sub> NPs. **b** The roughness images of BaTi<sub>1-x</sub>Zr<sub>x</sub>O<sub>3</sub> NPs. **c** Texture and roughness analysis of BaTi<sub>1-x</sub>Zr<sub>x</sub>O<sub>3</sub> NPs obtained from the FESEM images

$$R_a = \frac{1}{l} \int_0^l |Z(x)| dx \quad (3)$$

where  $l$  is length of the sample and  $Z(x)$  is the roughness profile coordinates. Whereas the root mean square roughness ( $R_q$ ) is calculated by using Eq. (4) [24]:

$$R_q = \sqrt{\frac{1}{l} \int_0^l |Z(x)|^2 dx} \quad (4)$$

Moreover, the maximum roughness height ( $R_t$ ), which is defined as the roughness profile's entire height, within the assessment length, ( $Z_p$ ) of the highest profile peak and the depth of the lowest profile valley ( $Z_v$ ), and given by Eq. (5)

$$R_t = Z_p + Z_v \quad (5)$$

These criteria are necessary for acquiring specific data, such as a scratch or an uncommon break in the material.

The collected data is finally tabulated in Table 1, and the prepared samples are perfect for the needed applications, such as photo-catalysis and heavy metal removal, because of their large surface area, high porosity, and appropriate roughness [23, 25].

### 3.3 Raman spectra (RS)

RS spectroscopy is a highly sensitive method used to examine the local structure of the atoms. The tetragonal BaTiO<sub>3</sub>



with a *P4* mm space group exhibits active vibration modes only, and each unit cell has five atoms and fifteen degrees of freedom. These are divided into the acoustical and optical branches represented by  $1F_{1u}$ , and  $3F_{1u} + 1F_{2u}$  symmetry modes, respectively.

The  $F_{1u}$  modes divide into modes of symmetry  $A_1 + E$ , and the  $F_{2u}$  mode divides into modes of symmetry  $B_1 + E$ . The  $A_1$  phonon modes are (IR) active for the exceptional ray (c- or Z-axis polarization), whereas the  $E$  modes are (IR) active for the ordinary ray (a- or X(y)-axis polarization). In the tetragonal phases of BaTiO<sub>3</sub>, the  $B_1$  symmetry mode is (IR) inactive.

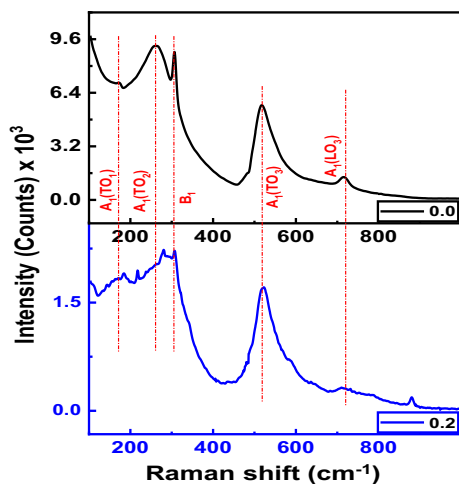
Additionally, long-range electrostatic forces also divide the  $A_1$  and  $E$  modes into transverse and longitudinal optical (TO and LO) modes [26].

Figure 3 illustrates the RS of the investigated samples BaTi<sub>1-x</sub>Zr<sub>x</sub>O<sub>3</sub>; (x=0.0, and 0.2) in the frequency range of 100–1000 cm<sup>-1</sup>. Table 2 provides a concise list of the identified Raman band locations and assignments for the two concentrations (x=0.0 and 0.2).

The peaks at 172, 263, and 518 cm<sup>-1</sup> for x=0.0 and 184, 281, and 523 cm<sup>-1</sup> for x=0.2 in Fig. 3 are allocated to the fundamental TO mode of the  $A_1$  symmetry, while the peak at 307 cm<sup>-1</sup> indicates asymmetry in the TiO<sub>6</sub> octahedra of BaTiO<sub>3</sub>. The weak peaks of about 715, and 711 cm<sup>-1</sup> for x=0.0 and x=0.2 respectively are linked to the greatest frequency LO mode with  $A_1$  symmetry.

The prepared samples show peaks at approximately 307 and 715 cm<sup>-1</sup>, confirming the system’s tetragonality [26, 27]. The emergence of the tetragonal phase in both samples is further indicated by the sharp peaks at 172, 263, and 518 cm<sup>-1</sup> for x=0.0 and the peaks at 184, 281, and 523 cm<sup>-1</sup> for x=0.2 [27].

When Zr<sup>4+</sup> is added to the BaTiO<sub>3</sub> structure, the basic TO mode of the  $A_1$  symmetry peak shifts to a higher



**Fig. 3** The Raman spectra for the BaTi<sub>(1-x)</sub>Zr<sub>(x)</sub>O<sub>3</sub>

**Table 2** The Raman band positions and corresponding band assignments of BaTi<sub>1-x</sub>Zr<sub>x</sub>O<sub>3</sub>, (x=0.0 and 0.2)

Composition	$A_1(TO_1)$ cm <sup>-1</sup>	$A_1(TO_2)$ cm <sup>-1</sup>	$B_1$ cm <sup>-1</sup>	$A_1(TO_3)$ cm <sup>-1</sup>	$A_1(LO_3)$ cm <sup>-1</sup>
x=0.0	172	263	307	518	715
x=0.2	184	281	307	523	711

wavenumber  $\gamma$ . This is due to a strong correlation between bond length (BL) and the Raman shift to higher  $\gamma$ . [28]. To confirm the previous hypothesis, the authors have to determine the (BL) between the Ti<sup>4+</sup> ions and the O<sup>2-</sup> ions at each of the two concentrations (0.0 and 0.2). The results of FTIR spectroscopy from the previous publication [20] were utilized to compute the bond length of the samples.

The vibrational frequency of the Ti–O bond is determined by the following equations [29, 30]:

$$\gamma = \frac{1}{2\pi c} \sqrt{\frac{k}{\mu}} \tag{6}$$

where  $\gamma$  is wave number,  $c$  is the speed of light,  $k$  and  $\mu$  are the average force constant and effective mass of the Ti–O bond respectively. The  $\mu$  is given by the [29]:

$$\mu = \frac{((1-x)m_{Ti} + (x)m_{Zr})m_O}{((1-x)m_{Ti} + (x)m_{Zr}) + m_O} \tag{7}$$

where  $m_{Ti}$ ,  $m_{Zr}$ , and  $m_O$  are the atomic masses of Ti, Zr, and O, respectively. The ( $k$ ) is linked to the average Ti–O bond length ( $r$ ) by the following relationship [30]:

$$r = \sqrt[3]{\frac{17}{k}} \tag{8}$$

The ( $\mu$ ), ( $k$ ), and Ti–O ( $r$ ), are given in Table 3.

From the table, one can notice that, the increase in the ( $\mu$ ) after doping is caused by the higher Zr atomic mass (91.224 u), compared to that of Ti (47.867 u). Moreover, the replacement of the Ti<sup>4+</sup> cation by a smaller Zr<sup>4+</sup> cation results in a movement of oxygen atoms closer to the metal cation, and a decrease in the length of the Ti–O bond along the ab plane. The decrease of the Ti–O BL leads to a higher bond stretching

**Table 3** The vibrational wave number of the (Ti–O) from FTIR spectra ( $\gamma$ ), effective mass ( $\mu$ ), force constant ( $k$ ), and the bond length ( $r_{Ti-O}$ ) for BaTi<sub>1-x</sub>Zr<sub>x</sub>O ceramics with x=0.0, and 0.2

Composition	$\gamma$ [20] cm <sup>-1</sup>	$\mu$ × 10 <sup>-26</sup> kg	$k$ N/cm	$r_{Ti-O}$ Å
x=0.0	557	1.9905	2.1913	1.9796
x=0.2	573	2.0701	2.4117	1.9174

frequency, which is a general view of Badger’s rule [29]. Consequently, the average force constant increases with Zr<sup>4+</sup> doping. The impact of the increase in (k) and (μ) leads to the detected Raman shifting of the fundamental T-O mode of the A<sub>1</sub> symmetry peak towards the higher frequency after doping, as shown in the Figure.

### 3.4 The optical measurements

#### 3.4.1 UV–visible absorption spectra

Figure 4:a depicts the spectrum of UV–Vis absorption of the samples versus the incident photons' wavelength (λ). The maximum absorption of BaTi<sub>1-x</sub>Zr<sub>x</sub>O<sub>3</sub> (0 ≤ x ≤ 0.3) is obtained at λ equals 342, 330, 360, and 324 nm, respectively.

The maximum absorption is attained for BaTi<sub>0.8</sub>Zr<sub>0.2</sub>O<sub>3</sub>, and the absorbance appears to slightly increase as the Zr content increases. The interaction of the samples with the incident photons starts to take place at the critical wavelengths λ<sub>0</sub> (listed in Table 4). The inset of Fig. 4a demonstrates how to obtain it for BaTi<sub>0.7</sub>Zr<sub>0.3</sub>O<sub>3</sub>.

The photon energy corresponding to the λ<sub>0</sub> is calculated from Eq. 9.

$$E_0(eV) = \frac{1239.83(eV \times nm)}{\lambda_0(nm)} \tag{9}$$

Thus, photons with energies lower than E<sub>0</sub> and ones greater than λ<sub>0</sub> cannot be absorbed by the samples. This issue gives us an idea about the transition nature of the samples. According to λ<sub>0</sub> and E<sub>0</sub> values, the sample BaTi<sub>0.8</sub>Zr<sub>0.2</sub>O<sub>3</sub> is the most responsive to incident photons with long λ and low energies as shown in the Table.

#### 3.4.2 The Kubelka–Munk (K-M) technique

The Kubelka–Munk (K-M) technique is utilized to obtain the optical energy gap (E<sub>g</sub>) of materials, and can be represented by the following equation [31]:

$$F(R) = \frac{(1 - R)^2}{2R} \tag{10}$$

where F(R) is the K-M function, which is proportional to the absorption coefficient (α), and R is the reflectance. A modified K-M function is expressed as (F(R) \* hv)<sup>1/n</sup>. The E<sub>g</sub> and the transition type can be identified by the well-known Tauc's equation [31, 32]:

$$\alpha(h\nu) = B(h\nu - E_g)^n \tag{11}$$

where ν is the light frequency, h is the Planck’s constant, B is the absorption constant, and (n) is the coefficient of an electronic transition.

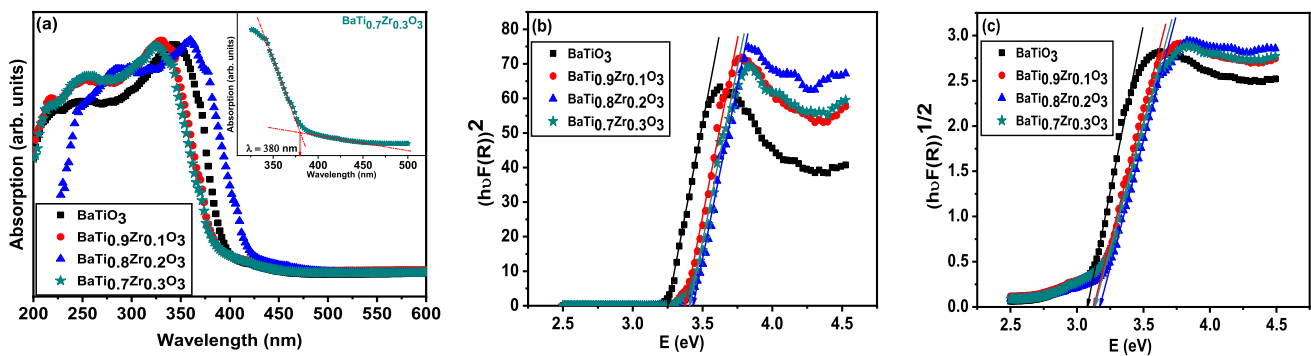


**Fig. 4** a UV–vis absorption spectra versus the wavelength of the incident photons, and b, c Tauc plots for estimating direct and indirect optical band gap for of BaTi<sub>(1-x)</sub>Zr<sub>(x)</sub>O<sub>3</sub>; (0.0 ≤ x ≤ 0.3)

**Table 4** The critical wavelength (λ<sub>0</sub>), the minimum photoenergy (E<sub>0</sub>), the direct optical energy gap (E<sub>g</sub>), of the samples BaTi<sub>1-x</sub>Zr<sub>x</sub>O<sub>3</sub> (0.0 ≤ x ≤ 0.3)

Composition	(K-M) Method				DASF Method	
	λ <sub>0</sub> (nm)	E <sub>0</sub> (eV)	Direct E <sub>g</sub> (eV)	Indirect E <sub>g</sub> (eV)	n	E <sub>g</sub> DASF (eV)
x=0.0	397	3.12	3.25	3.074	0.41	3.26
x=0.1	386	3.21	3.37	3.131	0.45	3.38
x=0.2	414	2.99	3.43	3.166	0.30	3.12
x=0.3	380	3.24	3.40	3.133	0.33	3.41

Tauc plots for BaTi<sub>1-x</sub>Zr<sub>x</sub>O<sub>3</sub>; (0 ≤ x ≤ 0.3) are shown in Fig. 4b, c. The E<sub>g</sub> of the investigated samples is obtained from the extrapolation of (F(R) \* hv)<sup>1/n</sup> to hv=0, for n equal to 1/2, and 2 to obtain the direct and indirect band gaps. Figure 4b depicts an allowable direct transition with an E<sub>g</sub> of approximately 3.25 eV for the virgin sample which is in line with values previously reported [33, 34].

It is clear that the values of E<sub>g</sub> increase with increasing Zr<sup>4+</sup> content. The reason for this trend may be due to some issues, among which is the contribution of the 3d orbitals of Zr ions [35]. It may also be ascribed to an increase in inter-atomic spacing that accompanied the increase in lattice volume [36]. Furthermore, by increasing the Zr<sup>4+</sup> concentration in the BaTiO<sub>3</sub>, the oxygen vacancies (OVs) increase and create more electrons that dwell in the minimal states near the conduction band's edge. A broadening in the band gap ΔE<sub>g</sub> happens as a consequence of an increase in the free charge carriers generated from OVs. This is referred to as the Burstein-Moss effect, and Eq. (12) back it up [36, 37]:

$$\Delta E_g = \left( \frac{\hbar^2}{2m_{vc}^*} \right) (3\pi^2 n)^{2/3} \tag{12}$$

where ΔE<sub>g</sub> is the shift of the doped BaTi<sub>1-x</sub>Zr<sub>x</sub>O<sub>3</sub> (0 ≤ x ≤ 0.3) relative to the pure BaTiO<sub>3</sub>, m<sub>vc</sub><sup>\*</sup>, ħ, and n are the reduced effective mass, the Planck's constant, and the charge carriers' concentration respectively [37].

### 3.4.3 The derivation of absorption spectrum fitting (DASF) technique

In the literature, it is difficult to categorize the electronic transition of BaTiO<sub>3</sub> as direct [33, 36, 38, 39], indirect [36], or both [34, 40, 41].

As seen in Fig. 4b and c, the linear fitting successfully matches the data for both curves in the examined samples. However, this matching cannot be relied upon solely. It is important to compare the direct and indirect E<sub>g</sub> with E<sub>0</sub> values in Table 4. It is possible to rule out the calculated E<sub>g</sub> value that is less than E<sub>0</sub> because it is out of the range of the absorbed energies [42].

The samples BaTi<sub>1-x</sub>Zr<sub>x</sub>O<sub>3</sub>; (0.0 ≤ x ≤ 0.3) are expected to have a direct band gap energy rather than the indirect, except the sample BaTi<sub>0.8</sub>Zr<sub>0.2</sub>O<sub>3</sub> may have both types of transition. Therefore, the authors resorted to the DASF to support the previous conclusion and to calculate the value of n (in Eq. (13)) which identifies the type of transition. To obtain the E<sub>g</sub> via the DASF technique, Eq. (11) can be expressed in terms of photons' wavelengths λ as follows [43]:

$$\alpha(\lambda) = B * (hc)^{n-1} * \lambda \left( \frac{1}{\lambda} - \frac{1}{\lambda_g} \right)^n \tag{13}$$

where α(λ) is the absorption coefficient equals (2.303/Z)A where, A is the sample's absorbance and Z is the sample's thickness provided by Beer–Lambert's law. The λ<sub>g</sub>, h, and c are wavelengths associated with the optical gap obtained by the DASF method (E<sub>g</sub><sup>DASF</sup>), Planck's constant, and the speed of light, respectively.

Thus, the Eq. (13) can be rearranged as follows [43]:

$$\frac{A(\lambda)}{\lambda} = D \left( \frac{1}{\lambda} - \frac{1}{\lambda_g} \right)^n \tag{14}$$

where D is a constant =  $\frac{B*(hc)^{n-1}*Z}{2.303}$

Applying the natural logarithm (Ln) for both sides to estimate n and λ<sub>g</sub> values [43].

$$\text{Ln} \left[ \frac{A(\lambda)}{\lambda} \right] = \text{Ln}(D) + n \text{Ln} \left( \frac{1}{\lambda} - \frac{1}{\lambda_g} \right) \tag{15}$$

To estimate n values, first λ<sub>g</sub> must be determined by taking the first derivative of Eq. (15) with respect to 1/λ and then plotting the  $\frac{d\{\text{Ln}[\frac{A(\lambda)}{\lambda}]\}}{d(\frac{1}{\lambda})}$  versus 1/λ. The value of λ<sub>g</sub> can be identified as demonstrated in Fig. 5a–d for all samples.

The first derivative of Eq. (15) can be expressed as follows [43]:

$$\frac{d\{\text{Ln}[\frac{A(\lambda)}{\lambda}]\}}{d(\frac{1}{\lambda})} = \frac{n}{(\frac{1}{\lambda} - \frac{1}{\lambda_g})} \tag{16}$$

The λ<sub>g</sub> value can then be substituted for each sample in Eq. (15) separately and plotted as the relation between Ln [  $\frac{A(\lambda)}{\lambda}$  ] and Ln(  $\frac{1}{\lambda} - \frac{1}{\lambda_g}$  ) as shown in Fig. 5e.

The slope of the fitted linear part equals n, which is listed in Table 4. It is approximately equal to 0.5 for all samples, indicating a direct transition [43].

Furthermore, the energy gaps (E<sub>g</sub><sup>DASF</sup> =  $\frac{1239.83}{\lambda_g}$ ) corresponding to every λ<sub>g</sub> are calculated and listed in the Table The calculated E<sub>g</sub><sup>DASF</sup> most nearly matches with the calculated E<sub>g</sub> obtained from the K-M method except for the doped sample with x = 0.2.

### 3.4.4 The optical applications

Thermodynamically, in order to use a semiconductor in a particular application, the reduction–oxidation potentials of the reaction must lie between the valence potential and the conduction potential of the semiconductor.

First, the valence band (VB) and conduction band (CB) are recognized with regard to the normal hydrogen electrode (NHE) scale at pH = 0. The Mulliken electronegativity rules are considered and follow the following equations [44, 45]:

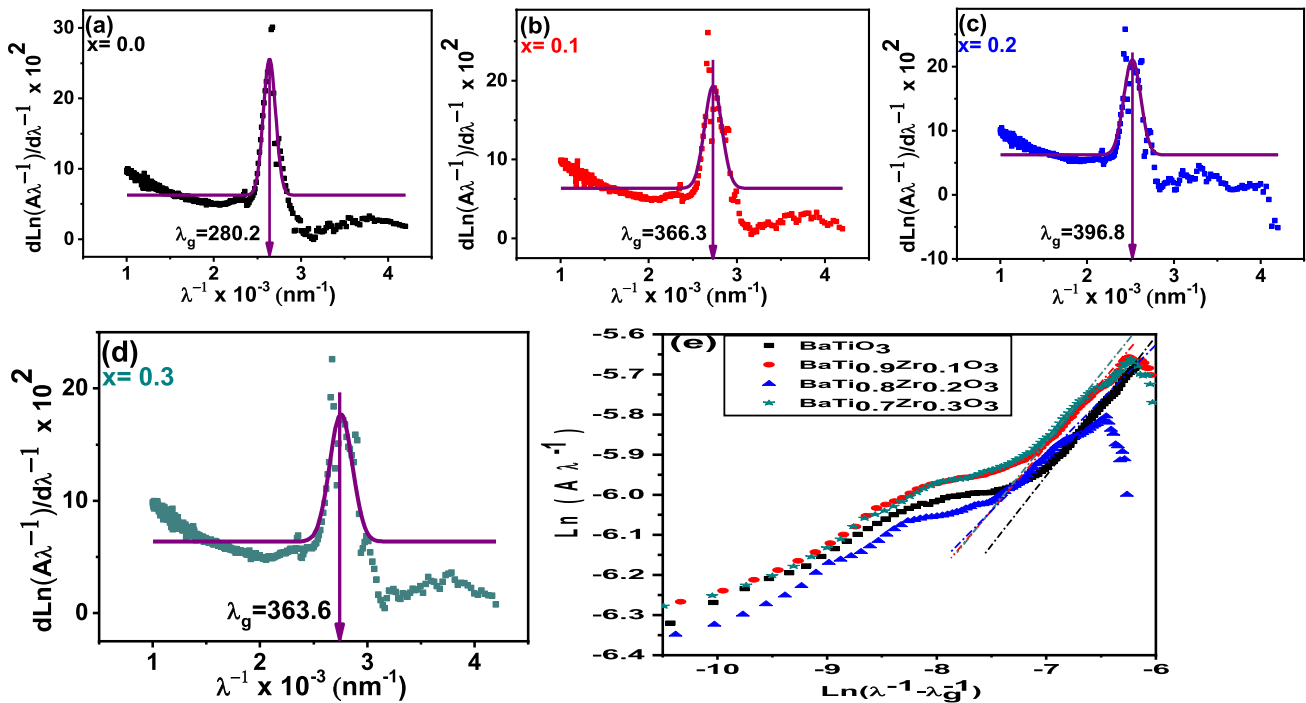


**Fig. 5** a–d DASF Plot of  $d\{\ln(A/\lambda)\}/d(1/\lambda)$  versus  $(1/\lambda)$ , e DASF plot of  $\ln(A/\lambda)$  versus  $\ln(\lambda^{-1}-\lambda_g^{-1})$  for  $\text{BaTi}_{(1-x)}\text{Zr}_x\text{O}_3$ ; ( $0.0 \leq x \leq 0.3$ )

$$E_{CB} = \chi - E^e - \frac{1}{2}E_g \tag{17} \quad \chi_{atom} = \frac{1}{2}(A_f + I_1) \tag{19}$$

$$E_{VB} = E_{CB} + E_g \tag{18}$$

where  $E_{CB}$  and  $E_{VB}$  are the CB, and VB potentials, respectively. The  $E^e$  is the free electron energy on the hydrogen scale ( $4.44 \pm 0.02\text{eV} \cong 4.45\text{eV}$ ) [45], and  $\chi$  represents the Mulliken's electronegativity (the bulk electronegativity), which equals [39]:

$\chi = (\chi_a^K \cdot \chi_b^L \cdot \chi_c^M \cdot \dots)^{\frac{1}{N}}$ , a, b, and c represent each atom in the compound. The K, L, and M represent the number of each atom in the compound, and N is the total number of atoms in the compound ( $= K + L + M + \dots$ ).

$\chi_{atom}$  for each atom determine by the following expression [47]:

where  $A_f$  is the atomic electron affinity (the absolute value is considered in eV), and  $I_1$  is the first ionization potential in eV,  $A_f$  and  $I_1$  are constants for each atom and their values are tabulated in Table 5 (kJ/mol).

For our calculations for the examined samples of the formula  $\text{BaTi}_{1-x}\text{Zr}_x\text{O}_3$ ; ( $0 \leq x \leq 0.3$ ), we set [ $\chi = (\chi_{Ba}^1 \cdot \chi_{Ti}^{1-x} \cdot \chi_{Zr}^x \cdot \chi_O^3)^{\frac{1}{5}}$ ]. For the reader's convenience, some calculations are provided below in detail, and the Table contains a list of the other results.

$$\chi_{Ba} = \frac{1}{2} \left( |-14| \frac{1\text{eV}}{96.48 \frac{\text{kJ}}{\text{mol}}} + 502.9 \frac{1\text{eV}}{96.48 \frac{\text{kJ}}{\text{mol}}} \right) = 2.68\text{eV} \quad ,$$

( $1\text{eV} = 96.48\text{kJ/mol}$ ), and similarly for Ti, Zr, and O atoms.

**Table 5** Calculations and results of positions of the valance band (VB) and the conduction band (CB) edges

Calculations	Results							
	$A_f$ (kJ/mol)	$I_1$ (kJ/mol)	$\chi_{atom}$ (eV)	Composition	$\chi_x$ (eV)	CB (eV)	VB (eV)	
Ba	-14	502.9	2.68	x=0.0	5.246	-0.829	2.421	
Ti	-8	658.8	3.46	x=0.1	5.249	-0.886	2.484	
Zr	-41	640.1	3.53	x=0.2	5.251	K-M -0.914	DASF -0.759	K-M 2.516 2.361
O	-141	1313.9	7.54	x=0.3	5.253	-0.897	2.503	



$$\begin{aligned} \chi_{x=0.1} &= (\chi_{Ba}^1 \cdot \chi_{Ti}^{1-x} \cdot \chi_{Zr}^x \cdot \chi_O^3)^{\frac{1}{5}} \\ &= (2.68^1 \times 3.46^{0.9} \times 3.53^{0.1} \times 7.54^3)^{\frac{1}{5}} \\ &= 5.25 eV \end{aligned}$$

By substituting into the Eq. (17):

$$E_{CB(x=0.1)} = 5.25 - 4.45 - \frac{1}{2} \times 3.37 = -0.89 eV$$

By substituting into the Eq. (18):

$$E_{VB(x=0.1)} = -0.89 + 3.37 = 2.48 eV, \text{ and similarly for } x=0, 0.2 \text{ and } 0.3 \text{ compounds.}$$

The authors found that all samples are capable of performing overall water splitting and CO<sub>2</sub> reduction processes as shown in Fig. 6. For water splitting, the the VB potential is more positive than the redox potential of H<sub>2</sub>O/O<sub>2</sub> (1.23 eV), and the CB potential is more negative than the reduction of hydrogen proton potential H<sup>+</sup>/H<sub>2</sub> (0). All samples have a conduction potential for CO<sub>2</sub> reduction that is more negative than all CO<sub>2</sub> byproducts, such as HCOOH, HCHO, and CH<sub>4</sub> [35, 46].

### 3.5 Heavy metal removal (HMR)

#### 3.5.1 Effect of pH and Zr<sup>4+</sup> ion concentrations on HMR

The uptake behavior of (Cr<sup>6+</sup>) ions by Zr-doped BaTiO<sub>3</sub> NPs is examined at different pHs. Figure 7 demonstrates the adsorption behavior at various pH levels at room temperature (25° C).

The removal efficiency (η) of the examined samples is calculated using Eqs. (1, 2), as mentioned in the experimental section. Table 6 presents the η values for all samples at different pHs. It is clear that, in contrast to higher concentrations, the η of Cr<sup>6+</sup> at various pHs and the low concentrations of Zr<sup>4+</sup> do not exhibit great values. However, at low

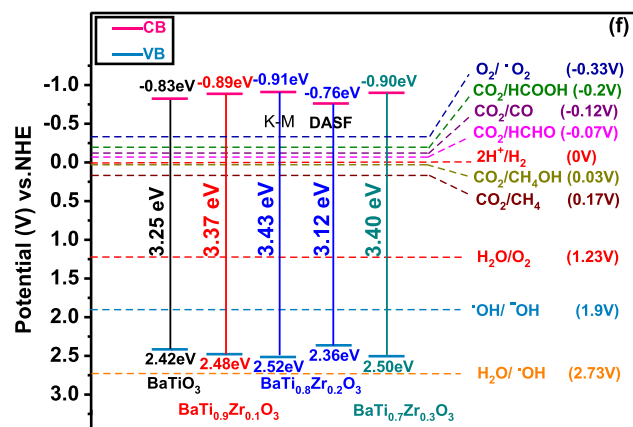


Fig. 6 The calculated band positions of CB and VB for BaTi<sub>(1-x)</sub>Zr<sub>(x)</sub>O<sub>3</sub>; (0 ≤ x ≤ 0.3); the CB and VB for x=0.2 are determined from E<sub>g</sub> using {(K-M) and (DASF)} methods

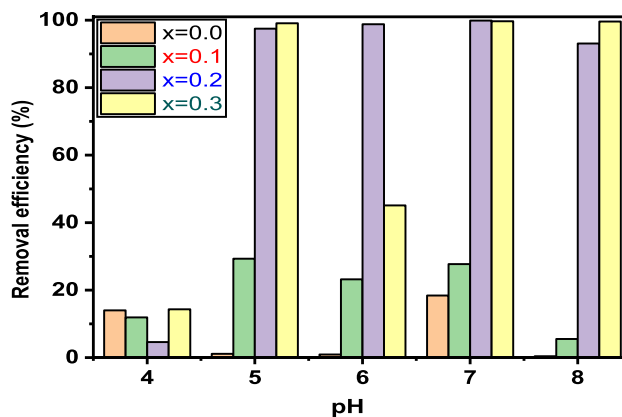


Fig. 7 Removal efficiency (%) of BaTi<sub>(1-x)</sub>Zr<sub>(x)</sub>O<sub>3</sub>; (0 ≤ x ≤ 0.3) NPs at different pH values

pH (pH = 4), the higher ion concentrations of Zr<sup>4+</sup> doped samples show lower values of η.

This can be attributed to the rivalry between H<sup>+</sup> and Cr<sup>6+</sup> over the accessible active sites of the adsorbent [16, 48]. The decrease in H<sup>+</sup>, is related to the increase in pH up to 7, resulting in more active sites accessible for Cr<sup>6+</sup> adsorption [49]. On the other hand, at a basic medium [pH > 7], OH<sup>-</sup> ions increase, Cr<sup>6+</sup> and Cr(OH)<sub>6</sub> are more readily adsorbed, and can be attached to the free binding sites [50]. As a result, the removal of Cr<sup>6+</sup> ions is related to both adsorption and precipitation. Finally, it can be seen that BaTi<sub>0.8</sub>Zr<sub>0.2</sub>O<sub>3</sub> has a higher η than other doped samples. This outcome is elucidated by the higher surface area and the smaller crystallite size.

The effect of pH is one of the most important factors that affects the process of HMR. Many researchers are interested in studying the effect of pH to determine the optimum value [51]. Seham Nagib et al. [52] used CALIX to investigate the influence of pH on vanadium extraction from different synthetic solutions. A series of studies were carried out at various hydrochloric acid concentrations ranging from 2 to 7.5 M. The results show that the vanadium extraction percentage increased as the pH increased up to 6–6.5 M before decreasing. This shows that the optimal acidity is 6 M.

Table 6 The HMR efficiency (%) of BaTi<sub>1-x</sub>Zr<sub>x</sub>O<sub>3</sub> (0.0 ≤ x ≤ 0.3) at different

x	pH 4	pH 5	pH 6	pH 7	pH 8
x=0.0	14.0	1.10	0.90	18.4	0.40
x=0.1	11.9	29.3	23.2	27.7	5.50
x=0.2	4.60	97.5	98.8	99.9	93.1
x=0.3	14.3	99.1	45.1	99.7	99.6

Magd M. Badr et al. investigated the influence of pH levels ranging from 2 to 7 on the adsorption of Ce(III) ions onto EPR1, EPR2, and EPR3 materials. The authors reported that the adsorption equilibrium was established at pH 4 [22].

### 3.5.2 Adsorption Isotherms study

Several models have been used to study the adsorption of HMR, including the Langmuir model, the Freundlich model, the Temkin model, and more [53]. Both the Langmuir and Freundlich models can be used to determine the adsorption capacity and affinity of the adsorbent material for the HM. However, the Freundlich model assumes multilayer adsorption and is more appropriate for heterogeneous adsorbent surfaces, whereas the Langmuir model assumes monolayer adsorption and is better suited for homogeneous adsorbent surfaces. Comparing the effectiveness of the Langmuir and Freundlich models can help to better understand the nature of the adsorption process and improve the design of the water treatment system [49]. In the case study, these approaches are used to investigate HM adsorption on Zr-doped BaTiO<sub>3</sub> NPs at various Cr<sup>6+</sup> ion concentrations.

#### 3.5.2.1 The Langmuir and Freundlich adsorption isotherms

The Langmuir and Freundlich isotherms models are used to clarify the adsorption process. Their models are expressed by Eqs. (20) and (21) respectively [54, 55]:

$$\frac{C_e}{q_e} = \frac{1}{k_l q_m} + \frac{C_e}{q_m} \tag{20}$$

$$\ln q_e = \ln k_f + \frac{1}{n} \ln C_e \tag{21}$$

where  $q_m$  (mg/g) is the maximum amount of HM that can be adsorbed per unit mass of adsorbent at equilibrium.  $k_l$  (L/mg) is the Langmuir adsorption coefficient, which is an indicator of the interaction's strength between the adsorbate and the adsorbent surface. On the other side, the  $K_f$  and  $n$  are physical constants signifying the adsorption capacity and intensity of adsorption, respectively.

Figure 8a and b displays the Langmuir and Freundlich isotherm models. As shown in the figures, using the slope of the straight line and the intercept with the Y-axis, the  $q_m$ ,  $k_l$ , and  $n$ ,  $k_f$  can be calculated from the Langmuir and Freundlich models respectively.

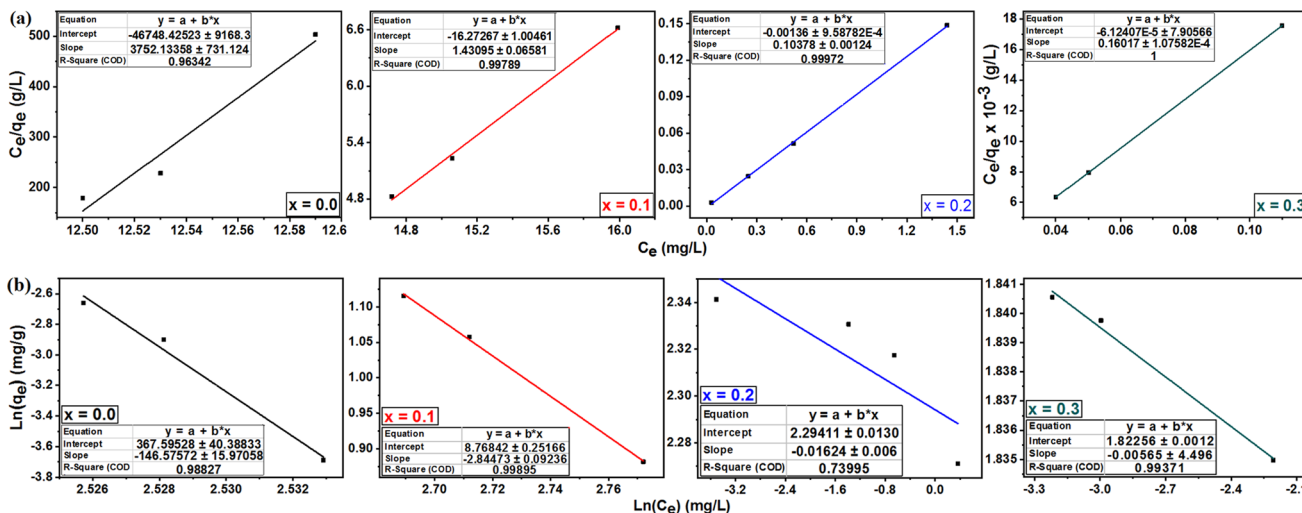


**Fig. 8** a, b Linear fit of experimental data on the adsorption of Cr<sup>6+</sup> onto BaTi<sub>(1-x)</sub>Zr<sub>(x)</sub>O<sub>3</sub>; (0.0 ≤ x ≤ 0.3) using the Langmuir and Freundlich adsorption isotherm models

**Table 7** The coefficients related to the adsorption capacity and strength constants of the adsorption isotherm models

Composition (x)	Langmuir isotherm			Freundlich isotherm		
	q <sub>m</sub> (mg/g)	k <sub>l</sub> (L/mg)	R <sup>2</sup>	n	k <sub>f</sub> (L/mg)	R <sup>2</sup>
0.0	2.67 × 10 <sup>-4</sup>	0.080	0.963	6.8 × 10 <sup>-3</sup>	–	0.988
0.1	0.699	0.090	0.998	0.350	–	0.999
0.2	9.620	74.290	0.999	61.60	9.97	0.739
0.3	6.250	0.026	1	177.0	6.05	0.994

Table 7 represents the coefficients regarding the adsorption capacity and strength constants of the adsorption isotherm models. From the table, it is clear that the doped sample for  $x=0.2$  has higher values of both  $q_m$  and  $k_l$  compared to the other samples.

However, the higher  $k_f$  value indicates a higher capacity for HMR, while a higher  $n$  value indicates stronger binding between the HM ions and the adsorbent material surface. The adsorption process is unfavorable if  $n < 1$ , it is favorable if ( $n > 1$ ), and it is irreversible if  $n = 1$  [21, 53, 56].

In the present case, the value of  $n$  for  $x=0.0$  and  $x=0.1$  is  $< 1$ , which indicates unfavorable adsorption on their surfaces. The obtained data is fully consistent with the low  $\eta$  of both samples compared to the other samples.

Finally, by looking at the values of the correlation coefficient ( $R^2$ ) in the table, one can conclude, that the Langmuir model is preferred for  $x=0.2$  and  $x=0.3$ . Therefore, adsorption of ( $\text{Cr}^{6+}$ ) on both surfaces followed monolayer adsorption [56]. While the Freundlich model can be proposed to describe the nature of adsorption at concentrations of  $x=0.0$  and  $x=0.1$ .

Additionally, according to the Langmuir model the sample at  $x=0.2$  has higher values of both  $q_m$  and  $k_l$  compared to the sample at  $x=0.3$ , indicating that it is the most efficient sample.

The  $\eta$  of HMR is influenced by many parameters, including size, surface roughness, and porosity. The smaller the sizes, the more efficient the removal of HMs. This is because smaller sizes have a higher surface area, which increases the rate of diffusion as well as the number of active sites that are available for adsorption. Additionally, the smaller sizes have a higher affinity for HMs, allowing them to bind more strongly and be more effectively removed [57].

Furthermore, the rougher surface can increase the removal efficiency of HMs by increasing the surface area available for adsorption and improving the contact between the surface and the HMs [58]. Samples at  $x=0.2$  and  $x=0.3$  have relatively low values of the crystallite size ( $L$ ) and are evidently rougher compared to other concentrations as detected in Table 1 and Fig. 2.

Table 8 compares the HM ion's adsorption capacity between  $\text{BaTi}_{1-x}\text{Zr}_x\text{O}_3$  ( $0.0 \leq x \leq 0.3$ ) and other adsorbents from the literature.

The  $\text{BaTi}_{0.8}\text{Zr}_{0.2}\text{O}_3$  sample has been used to successfully remove 99.9% of HMs ( $\text{Cr}^{6+}$ ) from wastewater.  $\text{BaTiO}_4$  materials have been developed by several authors for the HMR as shown in the table. The table shows that the investigated samples'  $\eta$  is higher than that of the majority of other adsorbents, making  $\text{BaTi}_{0.8}\text{Zr}_{0.2}\text{O}_3$  NPs a useful adsorbent for the removal of  $\text{Cr}^{6+}$  metal ions.

**Table 8** Comparison of maximal  $\text{Cr}^{6+}$  ion adsorption capacity by various adsorbents

Adsorbent	Removal efficiency (%)	Refs
Doped magnetite@SiO <sub>2</sub>	95	[13]
BiFeO <sub>3</sub> -Ni <sub>0.1</sub> Fe <sub>2.9</sub> O <sub>4</sub> nanocomposite	75	[16]
Ni ferrite/titanium oxide nanocomposite	97.2	[59]
SiO <sub>2</sub> /Ce <sub>2</sub> O <sub>3</sub>	55	[60]
NdFeO <sub>3</sub>	88	[61]
LaFeO <sub>3</sub>	84	[61]
SmFeO <sub>3</sub>	53	[61]
BaTiO <sub>3</sub> @SBA -15	98.8	[62]
Bulk BaTiO <sub>3</sub>	77.1	[62]
BaTi <sub>0.8</sub> Zr <sub>0.2</sub> O <sub>3</sub>	99.9	The present work

## 4 Conclusion

The perovskite samples  $\text{BaTi}_{1-x}\text{Zr}_x\text{O}_3$  ( $0 \leq x \leq 0.3$ ) were synthesized in a single phase using a modified citrate method. FESEM images illustrate that the NPs have a tetragonal shape with aggregation of grains, intragranular porosity, and roughness, which increase the surface area. The optical transition has been examined in several ways and the maximum absorption was observed for the sample  $\text{BaTi}_{0.8}\text{Zr}_{0.2}\text{O}_3$ . The perovskite samples  $\text{BaTi}_{1-x}\text{Zr}_x\text{O}_3$  ( $0 \leq x \leq 0.3$ ) have a direct allowed transition, and the band gap ( $E_g$ ) values improve as  $\text{Zr}^{4+}$  ion doping increases. The investigated samples can perform overall water splitting and CO<sub>2</sub> reduction processes.

Additionally, the  $\text{BaTi}_{0.8}\text{Zr}_{0.2}\text{O}_3$  sample achieves excellent results for heavy metal ( $\text{Cr}^{6+}$ ) removal from wastewater overall, and it also demonstrates far superior performance compared to previous investigations. The removal efficiency reaches 99.9% at pH 7 after 1 h.

**Author contributions** Mahasen Reda put the idea of the paper, material preparation, data collection and analysis, discussing the results of the structure, preparation of the first draft, and editing of the final manuscript, Ebtessam E. Ateia, S. I. El-Dek, and M. M. Arman, were sharing: planning; Data curation; Formal analysis; discussing the results of the structure, writing draft and revising final form.

**Funding** Open access funding provided by The Science, Technology & Innovation Funding Authority (STDF) in cooperation with The Egyptian Knowledge Bank (EKB). No funding was received.

**Data availability** All data that support the findings of this study are included within the article.

## Declarations

**Conflict of interest** The authors declare that they have no conflict of interest.

**Research data policy and data availability statements** Data will be available upon request.

**Open Access** This article is licensed under a Creative Commons Attribution 4.0 International License, which permits use, sharing, adaptation, distribution and reproduction in any medium or format, as long as you give appropriate credit to the original author(s) and the source, provide a link to the Creative Commons licence, and indicate if changes were made. The images or other third party material in this article are included in the article's Creative Commons licence, unless indicated otherwise in a credit line to the material. If material is not included in the article's Creative Commons licence and your intended use is not permitted by statutory regulation or exceeds the permitted use, you will need to obtain permission directly from the copyright holder. To view a copy of this licence, visit <http://creativecommons.org/licenses/by/4.0/>.

## References

1. F.M. Ahmed, E.E. Ateia, S.I. El-dek, S.M. Abd El-Kader, A.S. Shafaay, Synergistic interaction between molybdenum disulfide nanosheet and metal organic framework for high performance supercapacitor. *J. Energy Storage* **82**, 110360 (2024)
2. G. Liu, X.H. Wang, Y. Lin, L.T. Li, C.W. Nan, Growth kinetics of core-shell-structured grains and dielectric constant in rare-earth-doped BaTiO<sub>3</sub> ceramics. *J. Appl. Phys.* (2005). <https://doi.org/10.1063/1.2030413>
3. F.A. Ismail, R.A.M. Osman, M.S. Idris, Review on dielectric properties of rare earth doped barium titanate. *AIP Conf. Proc.* (2016). <https://doi.org/10.1063/1.4958786>
4. F. Ullah et al., Structural and dielectric studies of MgAl<sub>2</sub>O<sub>4</sub>-TiO<sub>2</sub> composites for energy storage applications. *Ceram. Int.* **47**(21), 30665–30670 (2021). <https://doi.org/10.1016/j.ceramint.2021.07.244>
5. N. Ullah et al., Effect of cobalt doping on the structural, optical and antibacterial properties of α-MnO<sub>2</sub> nanorods. *Appl. Phys. A Mater. Sci. Process.* **127**(10), 1–7 (2021). <https://doi.org/10.1007/s00339-021-04926-7>
6. M. Saleem et al., DFT and experimental investigations on CdTe1-xSex for thermoelectric and optoelectronic applications. *J. Alloys Compd.* **921**, 1–9 (2022). <https://doi.org/10.1016/j.jallcom.2022.166175>
7. T. Zeeshan et al., A comparative computational and experimental study of Al-ZrO<sub>2</sub> thin films for optoelectronic applications. *Solid State Commun. Commun.* **358**(November), 115006 (2022). <https://doi.org/10.1016/j.ssc.2022.115006>
8. M.T. Qureshi et al., Enhanced thermoelectric and optical response of Ag substituted Cu<sub>2</sub>O compositions for advanced applications. *Ceram. Int.* **49**(12), 19861–19869 (2023). <https://doi.org/10.1016/j.ceramint.2023.03.103>
9. F. Cao et al., Tuning dielectric loss of SiO<sub>2</sub>@CNTs for electromagnetic wave absorption. *Nanomaterials* **11**(10), 1–11 (2021). <https://doi.org/10.3390/nano11102636>
10. S.S. Kalanur, I.H. Yoo, K. Eom, H. Seo, Enhancement of photoelectrochemical water splitting response of WO<sub>3</sub> by means of Bi doping. *J. Catal.* **357**, 127–137 (2018). <https://doi.org/10.1016/j.jcat.2017.11.012>
11. P. Durga Prasad, J. Hemalatha, Dielectric and energy storage density studies in electrospun fiber mats of polyvinylidene fluoride (PVDF)/zinc ferrite (ZnFe<sub>2</sub>O<sub>4</sub>) multiferroic composite. *Phys. B Condens. Matter* **573**(July), 1–6 (2019). <https://doi.org/10.1016/j.physb.2019.08.023>
12. L. Zhou et al., Self-assembled core-shell CoFe<sub>2</sub>O<sub>4</sub>@BaTiO<sub>3</sub> particles loaded P(VDF-HFP) flexible films with excellent magneto-electric effects. *Appl. Phys. Lett.* **111**(3), 1–6 (2017). <https://doi.org/10.1063/1.4993161>
13. R. Ramadan, S.I. El-Dek, M.M. Arman, Enhancement of Mn-doped magnetite by mesoporous silica for technological application. *Appl. Phys. A Mater. Sci. Process.* **126**(11), 1–13 (2020). <https://doi.org/10.1007/s00339-020-04059-3>
14. S. Zinatloo-Ajabshir, M.S. Morassaei, M. Salavati-Niasari, Eco-friendly synthesis of Nd<sub>2</sub>Sn<sub>2</sub>O<sub>7</sub>-based nanostructure materials using grape juice as green fuel as photocatalyst for the degradation of erythrosine. *Compos. Part B Eng.* **167**(March), 643–653 (2019). <https://doi.org/10.1016/j.compositesb.2019.03.045>
15. S. Zinatloo-Ajabshir, M. Baladi, M. Salavati-Niasari, Sono-synthesis of MnWO<sub>4</sub> ceramic nanomaterials as highly efficient photocatalysts for the decomposition of toxic pollutants. *Ceram. Int.* **47**(21), 30178–30187 (2021). <https://doi.org/10.1016/j.ceramint.2021.07.197>
16. E.E. Ateia, O. Rabiea, A.T. Mohamed, Assessment of the correlation between optical properties and CQD preparation approaches. *Eur. Phys. J. Plus* **139**, 24 (2024)
17. A.I. Gopalan, K.P. Lee, K.M. Manesh, P. Santhosh, Poly(vinylidene fluoride)-polydiphenylamine composite electrospun membrane as high-performance polymer electrolyte for lithium batteries. *J. Memb. Sci.* **318**(1–2), 422–428 (2008). <https://doi.org/10.1016/j.memsci.2008.03.007>
18. T.M. Madumo, S.A. Zikalala, N.N. Gumbi, S.B. Mishra, B. Ntsendwana, E.N. Nxumalo, Development of nitrogen-doped graphene/MOF nanocomposites towards adsorptive removal of Cr(VI) from the wastewater of the Herbert Bickley treatment works. *Environ. Nanotechnol. Monit. Manag.* **20**(October 2022), 100794 (2023). <https://doi.org/10.1016/j.enmm.2023.100794>
19. J.Y. Liang et al., New insights into co-adsorption of Cr6+ and chlortetracycline by a new fruit peel based biochar composite from water: behavior and mechanism. *Colloids Surf A Physicochem Eng Asp Physicochem. Eng. Asp.* **672**(March), 131764 (2023). <https://doi.org/10.1016/j.colsurfa.2023.131764>
20. M. Reda, S.I. El-Dek, M.M. Arman, Improvement of ferroelectric properties via Zr doping in barium titanate nanoparticles. *J. Mater. Sci. Mater. Electron.* **33**(21), 16753–16776 (2022). <https://doi.org/10.1007/s10854-022-08541-x>
21. E.E. Ateia, M.A. Ateia, M.M. Arman, Assessing of channel structure and magnetic properties on heavy metal ions removal from water. *J. Mater. Sci. Mater. Electron.* **33**(11), 8958–8969 (2022). <https://doi.org/10.1007/s10854-021-07008-9>
22. M.M. Badr, W.M. Youssef, E.M. Elgammal, R.S. Abdel Hameed, M.M. El-Maadawy, A.E.M. Hussien, Investigating the efficiency of bisphenol-A diglycidyl ether/resole phenol formaldehyde/polyamine blends as Cerium adsorbent from aqueous solution. *J. Environ. Chem. Eng.* **11**(6), 111475 (2023). <https://doi.org/10.1016/j.jece.2023.111475>
23. E.E. Ateia, M.M. Arman, A.T. Mohamed, *Sci. Reports.* **13**, 3141 (2023). <https://doi.org/10.1038/s41598-023-30255-1>
24. S.M. Ghaseminezhad, M. Barikani, M. Salehirad, Development of graphene oxide-cellulose acetate nanocomposite reverse osmosis membrane for seawater desalination. *Compos. Part B Eng.* **161**, 320–327 (2019). <https://doi.org/10.1016/j.compositesb.2018.10.079>
25. E.E. Ateia, A.T. Mohamed, *Functionalized multimetal oxide-carbon nanotube-based nanocomposites and their properties*



- (Elsevier, 2022), pp.103–130. <https://doi.org/10.1016/B978-0-12-822694-0.00010-7>
26. C. Sameera Devi, G.S. Kumar, G. Prasad, Spectroscopic and electrical studies on Nd<sup>3+</sup>, Zr<sup>4+</sup> ions doped nano-sized BaTiO<sub>3</sub> ferroelectrics prepared by sol-gel method. *Spectrochim. Acta Part A Mol. Biomol. Spectrosc. Acta Part A Mol. Biomol. Spectrosc.* **136**(PB), 366–372 (2015). <https://doi.org/10.1016/j.saa.2014.09.042>
  27. U.A. Joshi, S. Yoon, S. Balk, J.S. Lee, Surfactant-free hydrothermal synthesis of highly tetragonal barium titanate nanowires: a structural investigation. *J. Phys. Chem. B* **110**(25), 12249–12256 (2006). <https://doi.org/10.1021/jp0600110>
  28. L. Popović, D. De Waal, J.C.A. Boeyens, Correlation between Raman wavenumbers and P-O bond lengths in crystalline inorganic phosphates. *J. Raman Spectrosc.* **36**(1), 2–11 (2005). <https://doi.org/10.1002/jrs.1253>
  29. U. Kumar et al., Fabrication of europium-doped barium titanate/polystyrene polymer nanocomposites using ultrasonication-assisted method: structural and optical properties. *Polymers (Basel)*. (2022). <https://doi.org/10.3390/polym14214664>
  30. H. Singh, K.L. Yadav, Structural, dielectric, vibrational and magnetic properties of Sm doped BiFeO<sub>3</sub> multiferroic ceramics prepared by a rapid liquid phase sintering method. *Ceram. Int.* **41**(8), 9285–9295 (2015). <https://doi.org/10.1016/j.ceramint.2015.03.212>
  31. R. López, R. Gómez, Band-gap energy estimation from diffuse reflectance measurements on sol-gel and commercial TiO<sub>2</sub>: a comparative study. *J. Sol-Gel Sci. Technol.* **61**(1), 1–7 (2012). <https://doi.org/10.1007/s10971-011-2582-9>
  32. E.E. Ateia, D. Gawad, M.M. Arman, Ab-initio study of structural, morphological and optical properties of multiferroic La<sub>2</sub>FeCrO<sub>6</sub>. *J. Alloys Compd. Compd* **976**(August 2023), 173017 (2024). <https://doi.org/10.1016/j.jallcom.2023.173017>
  33. A. Kheyrdan, H. Abdizadeh, A. Shakeri, M.R. Golobostanfard, Structural, electrical, and optical properties of sol-gel-derived zirconium-doped barium titanate thin films on transparent conductive substrates. *J. Sol-Gel Sci. Technol.* **86**(1), 141–150 (2018). <https://doi.org/10.1007/s10971-018-4610-5>
  34. C. Karunakaran, P. Vinayagamorthy, J. Jayabharathi, Optical, electrical, and photocatalytic properties of polyethylene glycol-assisted sol-gel synthesized BaTiO<sub>3</sub>@ZnO core-shell nanoparticles. *Powder Technol.* **254**, 480–487 (2014). <https://doi.org/10.1016/j.powtec.2014.01.061>
  35. Y. Ma et al., Electronic structures and optical properties of Fe/Co-doped cubic BaTiO<sub>3</sub> ceramics. *Ceram. Int.* **45**(5), 6303–6311 (2019). <https://doi.org/10.1016/j.ceramint.2018.12.113>
  36. S.C. Roy, G.L. Sharma, M.C. Bhatnagar, Large blue shift in the optical band-gap of sol-gel derived Ba<sub>0.5</sub>Sr<sub>0.5</sub>TiO<sub>3</sub> thin films. *Solid State Commun.* **141**(5), 243–247 (2007). <https://doi.org/10.1016/j.ssc.2006.11.007>
  37. S.M. Park, T. Ikegami, K. Ebihara, P.K. Shin, Structure and properties of transparent conductive doped ZnO films by pulsed laser deposition. *Appl. Surf. Sci.* **253**(3), 1522–1527 (2006). <https://doi.org/10.1016/j.apsusc.2006.02.046>
  38. D. Kothandan, R. Jeevan Kumar, K. Chandra Babu Naidu, Barium titanate microspheres by low temperature hydrothermal method: Studies on structural, morphological, and optical properties. *J. Asian Ceram. Soc.* **6**(1), 1–6 (2018). <https://doi.org/10.1080/21870764.2018.1439607>
  39. H.K. El Emam, S.I. El-Dek, W.M.A. El Rouby, Aerosol spray assisted synthesis of Ni doped BaTiO<sub>3</sub> hollow porous spheres/graphene as photoanode for water splitting. *J. Electrochem. Soc. Electrochem. Soc.* **168**(5), 050540 (2021). <https://doi.org/10.1149/1945-7111/ac001e>
  40. S. Sagadevan, J. Podder, Investigation of structural, SEM, TEM and dielectric properties of BaTiO<sub>3</sub> nanoparticles. *J. Nano-Electron. Phys.* **7**(4), 2–6 (2015)
  41. T.A. Khalyavka, N.D. Shcherban, V.V. Shymanovska, E.V. Manuilov, V.V. Permyakov, S.N. Shcherbakov, Cerium-doped mesoporous BaTiO<sub>3</sub>/TiO<sub>2</sub> nanocomposites: structural, optical and photocatalytic properties. *Res. Chem. Intermed.* **45**(8), 4029–4042 (2019). <https://doi.org/10.1007/s11164-019-03888-z>
  42. Q.A. Mohammed, Z.R. Ali, A.F. Mijbas, Electrical and optical properties of dielectric BaTiO<sub>3</sub> single crystals prepared by flux technique. *J. Babylon Univ. Sci.* **20**(1), 149–160 (2005)
  43. D. Souri, Z.E. Tahan, A new method for the determination of optical band gap and the nature of optical transitions in semiconductors. *Appl. Phys. B Lasers Opt.* **119**(2), 273–279 (2015). <https://doi.org/10.1007/s00340-015-6053-9>
  44. A. Habibi-Yangjeh, M. Shekofteh-Gohari, Novel magnetic Fe<sub>3</sub>O<sub>4</sub>/ZnO/NiWO<sub>4</sub> nanocomposites: enhanced visible-light photocatalytic performance through p-n heterojunctions. *Sep. Purif. Technol.* **184**, 334–346 (2017). <https://doi.org/10.1016/j.seppur.2017.05.007>
  45. S. Mahajan, O.P. Thakur, C. Prakash, K. Sreenivas, Effect of Zr on dielectric, ferroelectric and impedance properties of BaTiO<sub>3</sub> ceramic. *Bull. Mater. Sci.* **34**(7), 1483–1489 (2011). <https://doi.org/10.1007/s12034-011-0347-2>
  46. A.M.A.A.S. Yong Xu, The absolute energy positions of conduction and valence bands of selected semiconducting minerals. *Am. Mineral.* **85**(3–4), 543–556 (2000)
  47. S. Shenoy, K. Tarafder, Enhanced photocatalytic efficiency of layered CdS/CdSe heterostructures: insights from first principles electronic structure calculations. *J. Phys. Condens. Matter* **32**(27), 8–14 (2020). <https://doi.org/10.1088/1361-648X/ab7b1c>
  48. M.K. Ahmed, R. Ramadan, S.I. El-dek, V. Uskoković, Complex relationship between alumina and selenium-doped carbonated hydroxyapatite as the ceramic additives to electrospun polycaprolactone scaffolds for tissue engineering applications. *J. Alloys Compd.* **801**, 70–81 (2019). <https://doi.org/10.1016/j.jallcom.2019.06.013>
  49. E.E. Ateia, D.E. El-Nashar, R. Ramadan, M.F. Shokry, Synthesis and characterization of EPDM/ferrite nanocomposites. *J. Inorg. Organomet. Polym. Mater.* **30**(4), 1041–1048 (2020). <https://doi.org/10.1007/s10904-019-01237-6>
  50. E.E. Ateia, R. Elraaie, A.T. Mohamed, Designing bi-functional Ag-CoGd<sub>0.025</sub>Er<sub>0.05</sub>Fe<sub>1.925</sub>O<sub>4</sub> nanoarchitecture via green method. *J. Phys. D Appl. Phys.* (2024). <https://doi.org/10.1088/1361-6463/ad1f31>
  51. R.S. Abdel Hameed, A.H. Al Bagawi, H. AljuhianiEnas, O.A. Farghaly, Application of electro analytical in trace metals determinations: environmental and industrial samples, review article. *Determine. Nanomed. Nanotechnol.* **2**(3), DNN.000536 (2021). <https://doi.org/10.31031/DNN.2021.02.000536>
  52. S. Nagib, R.S. Abdel Hameed, Recovery of vanadium from hydrodesulfurization waste catalyst using calix[4] resorcinarenes. *Green Chem. Lett. Rev.* **10**(4), 210–215 (2017). <https://doi.org/10.1080/17518253.2017.1348543>
  53. X. Chen et al., Isotherm models for adsorption of heavy metals from water—a review. *Chemosphere* **307**(P1), 135545 (2022). <https://doi.org/10.1016/j.chemosphere.2022.135545>
  54. E.E. Ateia, D. Gawad, M. Mosry, M.M. Arman, Synthesis and functional properties of La<sub>2</sub>FeCrO<sub>6</sub> based nanostructures. *J. Inorg. Organometall. Polym. Mater.* (2023). <https://doi.org/10.1007/s10904-023-02699-5>. (Published online 22 May 2023)
  55. S. Shukrullah, M. Azam, M.Y. Naz, I. Toqeer, A. Gungor, Effective removal of chromium from wastewater with Zn doped Ni



- ferrite nanoparticles produced using co-precipitation method. *Mater. Today Proc.* **47**(xxxx), S9–S12 (2020). <https://doi.org/10.1016/j.matpr.2020.04.263>
56. O.S. Alkhazrajy, M.H. Abdul-Latif, M.A. Al-Abayaji, Adsorption of metoclopramide hydrochloride onto burned initiated Iraqi bentonite. *J. Al-Nahrain Univ. Sci.* **15**(2), 35–46 (2012). <https://doi.org/10.22401/jnus.15.2.05>
57. M.M. Arman, Synthesis, characterization, magnetic properties, and applications of  $\text{La}_{0.85}\text{Ce}_{0.15}\text{FeO}_3$  perovskite in heavy metal  $\text{Pb}^{2+}$  removal. *J. Supercond. Nov. Magn.* **35**(5), 1241–1249 (2022). <https://doi.org/10.1007/s10948-022-06168-x>
58. C. Qiu, C. Panwisawas, M. Ward, H.C. Basoalto, J.W. Brooks, M.M. Attallah, On the role of melt flow into the surface structure and porosity development during selective laser melting. *Acta Mater.* **96**(May 2019), 72–79 (2015). <https://doi.org/10.1016/j.actamat.2015.06.004>
59. H. Shekari, M.H. Sayadi, M.R. Rezaei, A. Allahresani, Synthesis of nickel ferrite/titanium oxide magnetic nanocomposite and its use to remove hexavalent chromium from aqueous solutions. *Surfaces Interfaces* **8**, 199–205 (2017). <https://doi.org/10.1016/j.surfin.2017.06.006>
60. Y.A. Saeid, E.E. Ateia, Efficient removal of Pb (II) from water solution using  $\text{CaFe}_{2-x-y}\text{Gd}_x\text{Sm}_y\text{O}_4$  ferrite nanoparticles. *Appl. Phys. A* **128**, 583 (2022). <https://doi.org/10.1007/s00339-022-05718-3>
61. M.M. Arman, The effect of the rare earth A-site cation on the structure, morphology, physical properties, and application of perovskite  $\text{AFeO}_3$ . *Mater. Chem. Phys.* **304**(April), 127852 (2023). <https://doi.org/10.1016/j.matchemphys.2023.127852>
62. V. Kumari, M. Sasidharan, A. Bhaumik, Mesoporous  $\text{BaTiO}_3@$ SBA-15 derived via solid state reaction and its excellent adsorption efficiency for the removal of hexavalent chromium from water. *Dalt. Trans.* **44**(4), 1924–1932 (2015). <https://doi.org/10.1039/c4dt03180f>

**Publisher's Note** Springer Nature remains neutral with regard to jurisdictional claims in published maps and institutional affiliations.